Application of an Efficient Hybrid Scheme for Aeroelastic Analysis of Advanced Propellers

R. Srivastava* and Lakshmi N. Sankar†
Georgia Institute of Technology, Atlanta, Georgia 30332
T. S. R. Reddy‡
University of Toledo, Toledo, Ohio 43606
and
D. L. Huff§
NASA Lewis Research Center, Cleveland, Ohio 44135

An efficient three-dimensional hybrid scheme is applied for solving Euler equations to analyze advanced propellers. The scheme treats the spanwise direction semiexplicitly and the other two directions implicitly, without affecting the accuracy, as compared to a fully implicit scheme. This leads to a reduction in computer time and memory requirement. The calculated power coefficients for two advanced propellers, SR3 and SR7L, at various advance ratios showed good correlation with experiment. Spanwise distribution of elemental power coefficient and steady pressure coefficient differences also showed good agreement with experiment. A study of the effect of structural flexibility on the performance of the advanced propellers showed that structural deformation due to centrifugal and aeroloading should be included for better correlation. The study also showed that adjustments to the setting angle by rigid-body rotation does not simulate the correct blade shape.

Nomenclature

A, B = flux Jacobian matrices
D_E = explicit dissipation terms
D_{I_ξ}, D_{I_ζ} = implicit dissipation terms
$\boldsymbol{E}, \boldsymbol{F}, \boldsymbol{G}$ = flux vectors in computational plane
$\hat{\boldsymbol{E}}, \hat{\boldsymbol{F}}, \hat{\boldsymbol{G}}$ = flux vectors in physical plane
e = total energy per unit volume
I = identity matrix
J = Jacobian of transformation
$[\boldsymbol{K}(\Omega)_s]$ = centrifugal softening matrix
$[\boldsymbol{K}(u)]$ = nonlinear stiffness matrix
n = current time level
$n + 1$ = next time level
$\boldsymbol{n}$ = unit surface normal
$\{\boldsymbol{P}(u)\}$ = equivalent aerodynamic force vector
p = pressure
$\boldsymbol{q}$ = flow properties vector in computational plane
$\hat{\boldsymbol{q}}$ = flow properties vector in physical plane
$\boldsymbol{R}$ = residual vector
t = time
u, v, w = Cartesian velocity components
$\{u\}$ = blade deflections at finite element nodes
U, V, W = contravariant velocity components
V_b = velocity vector on the boundary
x, y, z = coordinate direction in physical plane
β = blade setting angle (twist at 75% span)
γ = ratio of specific heats
Δ = forward-difference operator
δ = central-difference operator
ε_E = explicit dissipation coefficient
ε_I = implicit dissipation coefficient
ρ = density
ξ, η, ζ = coordinate direction in computational plane
ξ_t, ξ_x, η_x, etc. = metrics of transformation
τ = time in computational plane
$\Omega\%$ = rotational speed

Presented as Paper 90-0028 at the 28th Aerospace Sciences Meeting, Reno, NV, Jan. 8–11, 1990; received Jan. 22, 1990; revision received June 30, 1990; accepted for publication July 9, 1990.

*Graduate Student; currently Resident Research Associate at NASA Lewis Research Center. Member AIAA.
†Associate Professor. Member AIAA.
‡NASA Resident Research Associate at Lewis Research Center. Member AIAA.
§Research Engineer. Member AIAA.

Introduction

CURRENTLY an effort is underway to improve the propulsive efficiency of commercial and military aircraft. Newly designed high-speed advanced propellers, also known as propfans, show a very high propulsive efficiency at cruise speeds up to Mach 0.8.[1] The propfans are designed to delay the compressibility losses, by sweeping the blade backwards and using thinner airfoils, on the outboard section of the blade. In addition low-aspect-ratio blades are used. This, combined with high tip Mach number, leads to high blade twist and high disk loading. The requirement of high disk loading further dictates a large number of blades per propeller, which must maintain structural integrity. However, these special features of the propfans lead to new problems, namely large amplitude oscillations due to their flexibility, transonic classical flutter due to high sweep at the tips, and unstable behavior due to aerodynamic coupling (cascade effects).[2]

To understand and alleviate the problems associated with the propfan, the flow phenomena on the blades have to be accurately known, either through experimental or numerical techniques. At the design stage experimental techniques are very expensive. Therefore, a need definitely exists to support the development of potentially high propulsive efficiency propfans through numerical techniques.

The existing numerical methods vary in complexity from simple Goldstein-type strip analysis to analyses that solve the Euler and Navier-Stokes equations. The strip theory based

on Goldstein's work[3] assumes the flow to be inviscid and incompressible (hence irrotational). The propeller is modeled by a lifting line vortex and the wake is assumed to be composed of a rigid helical vortex sheet. In this analysis, the propeller is restricted to having straight blades and no provision can be made for the nacelle, since the vortex wake extends to the axis. Sullivan[4] has improved on this method by using the curved lifting line concept to account for the sweep. In this approach, the vortex wake is represented by a finite number of vortex filaments in place of the continuous sheet of vorticity as used in Goldstein's approach. The analysis has been further extended in Ref. 5 by placing the vortex filaments along the stream surfaces so that they conform to the shape of the axisymmetric nacelle.

Hanson[6] and Williams and Hwang[7] applied the Kernel-function approach to a propfan blade. They numerically solve a linear equation for upwash angle due to the blade pressure distribution by discretizing the load representation. The friction drag is obtained from the two-dimensional airfoil tables as a function of lift coefficient for the appropriate section camber, thickness, and a Mach number adjusted for sweep and three-dimensional effects. The induced drag is obtained by determining the kinetic energy per unit length of the far wake. The methods mentioned so far are based on linearized analyses. However, as the advanced propeller operates at or near transonic tip Mach number, flow nonlinearities may become important, requiring advanced methods of analysis.

Jou[8] has applied the finite-volume approach of Jameson and Caughy[9] for the analysis of propfans using the full-potential equation. The formulation was not able to provide converged solutions for freestream Mach numbers greater than 0.6. It was concluded that strong rotational flow effects were present near the leading edge, which could not be modeled by the potential equation. In addition, the potential flow equations at times lead to nonunique solutions.

Chaussee[10] and Whitfield *et al.*[11] have applied the unsteady, three-dimensional Euler equations to the propfan geometry. Matsuo *et al.*[12] have recently solved the full Navier-Stokes equations around a propfan. Some of these methods have been reviewed with regards to performance prediction.[13]

All of the analyses mentioned so far, with the exception of Whitfield *et al.*[11] have been for axisymmetric flows. However, a true unsteady analysis would permit the analysis of the propfan in all flight configurations, including climb and descent, at off-design conditions such as gusts or cross winds due to the disturbances in the atmosphere.

The primary objective of the present research is to develop a method to solve unsteady Euler equations to predict flowfield around a propfan in nonaxisymmetric flight condition, undergoing a time-dependent forcing function, unsteady blade vibratory motion, etc. To accomplish this objective, a versatile body-fitted grid is used. The blade motion is simulated by grid motion, allowing any time-dependent blade motion. This permits the calculation of both forced and free response due to any time-dependent forcing function for a flexible blade. It also allows the governing equations to be cast in Cartesian coordinates, and yet be able to simulate a rotating blade. A Cartesian grid system simplifies the governing equations, as the Coriolis forces do not appear explicitly. This is true not only for a rotating blade but also for a blade undergoing a time-dependent arbitrary motion.

The governing equations in fully conservative form are discretized using second-order accurate central differencing for the spatial derivatives and a first-order upwind differencing for the temporal derivative, to obtain a set of algebraic equations. The alternating direction implicit (ADI) scheme is used to solve the algebraic equations. The radial direction fluxes are treated semiexplicitly, and the other two directions implicitly, without affecting the accuracy significantly as compared to a fully implicit scheme. Treating one direction semiexplicitly requires only two costly inversions of block tridiagonal matrix, as opposed to three inversions for a fully implicit scheme, per time step. It also reduces the memory requirement as only two time levels of information needs to be stored at any given time, one of which needs to be only two-dimensional. The use of such a hybrid scheme leading to reduction in computer time and memory requirement makes the scheme more efficient.

The specific objectives of the present paper are 1) to apply an efficient hybrid scheme to analyze advanced propellers; 2) to calculate steady performance; 3) to include structural deformation, due to centrifugal and steady aeroloading in the analysis; and 4) to study the effects of structural flexibility on the performance of advanced propellers. The governing equations and the numerical solution method described are applicable to both axisymmetric and nonaxisymmetric flow conditions. However, in the present work only axisymmetric flow is considered due to very high computational cost involved in analyzing a nonaxisymmetric flight condition. Furthermore, reliable experimental data is available only for axisymmetric flight. The methods developed here are expected to be helpful for future aeroelastic research.

Formulation

Aerodynamic Model

The Euler equations, in conservation form, in Cartesian coordinate system can be written as

$$(\hat{q})_t + (\hat{E})_x + (\hat{F})_y + (\hat{G})_z = 0 \tag{1}$$

$\hat{E}$, $\hat{F}$, and $\hat{G}$ are the nonlinear flux vectors which are functions of the vector $\hat{q}$. The subscripts denote the partial derivative of the vector. In the above equation

$$\hat{q} = \{\rho, \rho u, \rho v, \rho w, e\}^T \tag{2a}$$

$$\hat{E} = \{\rho u, \rho u^2 + p, \rho uv, \rho uw, u(e + p)\}^T \tag{2b}$$

$$\hat{F} = \{\rho v, \rho uv, \rho v^2 + p, \rho vw, v(e + p)\}^T \tag{2c}$$

$$\hat{G} = \{\rho w, \rho uw, \rho vw, \rho w^2 + p, w(e + p)\}^T \tag{2d}$$

p, the hydrodynamic pressure, may be expressed using the equation of state for perfect gas as

$$p = (\gamma - 1)\left[e - \frac{1}{2}\rho(u^2 + v^2 + w^2)\right] \tag{3}$$

The advantage of using the conservation form is that it ensures the conservation of physical flux properties across discontinuities (e.g., shock) in the flow.[14]

In order to analyze flow past an arbitrary geometry undergoing arbitrary motion, these equations need to be transformed and recast in a generalized coordinate system. The coordinates of the generalized system have the following one-to-one relationship with the coordinates in the physical domain of interest:

$$\xi = \xi(x, y, z, t), \qquad \eta = \eta(x, y, z, t),$$
$$\zeta = \zeta(x, y, z, t), \qquad \tau = t \tag{4}$$

These coordinates are nonorthogonal and completely general. Equation (1) can then be rewritten as

$$q_\tau + E_\xi + F_\eta + G_\zeta = 0 \tag{5}$$

where

$$q = J^{-1}\{\rho, \rho u, \rho v, \rho w, e\}^T \tag{6a}$$

$$\mathbf{E} = J^{-1}\{\rho U,\ \rho uU + \xi_x p,\ \rho vU + \xi_y p,\ \rho wU + \xi_z p,\ (e + p)U - \xi_t p\}^T \quad (6b)$$

$$\boldsymbol{F} = J^{-1}\{\rho V,\ \rho uV + \eta_x p,\ \rho vV + \eta_y p,\ \rho wV + \eta_z p,\ (e + p)V - \eta_t p\}^T \quad (6c)$$

$$\boldsymbol{G} = J^{-1}\{\rho W,\ \rho uW + \zeta_x p,\ \rho vW + \zeta_y p,\ \rho wW + \zeta_z p,\ (e + p)W - \zeta_t p\}^T \quad (6d)$$

Initial and Boundary Conditions

The initial conditions may be critical to convergence of the numerical scheme. For the calculations presented here, the freestream conditions are used as the initial conditions.

In the present analysis, the flow variables at the boundaries are updated explicitly after the governing equations have been solved for the interior flowfield. The following boundary conditions need to be addressed:

The Blade and Nacelle-Surface Boundary Condition

Physically, there can be no flow through or on a solid surface, hence the velocity on a solid surface must go to zero. The physical boundary condition of no slip can be ignored for the Euler equations. Thus, the boundary condition on the blade and nacelle surfaces can be mathematically written as

$$\boldsymbol{V}_b \cdot \boldsymbol{n} = 0 \quad (7)$$

Far-Field Conditions

Since the propfan is operating in free air, the far-field conditions should be the same as that of the free air. For steady-state calculations, all disturbances from the solid surface must propagate to infinity. On the subsonic inflow boundary, one characteristic should be allowed to escape hence ρ is extrapolated and the remaining variables ρu, ρv, ρw, and e are fixed at the freestream value. For a supersonic inflow boundary, all quantities are fixed to that of the freestream, as disturbances cannot travel upstream in a supersonic flow. At the subsonic outflow boundary, four characteristics should escape, thus the four quantities ρ, ρu, ρv, and ρw are extrapolated from inside while the pressure is fixed to that of the freestream. For supersonic outflow, all characteristics should escape, hence all quantities are extrapolated from inside the flow domain.

The Block Interface Boundary

It is neither efficient nor practical to solve all of the blades at the same time, hence, one blade passage is handled at a time. This introduces additional boundaries for computation. Across these boundaries all the variables must be continuous, except on solid boundaries and boundaries downstream of the blade. The boundary condition, for these boundaries, depends on the type of flow being solved. An axisymmetric flow would require periodicity on the fluid interface boundaries. Periodicity will require that the two boundaries have same fluid properties. As shown in Fig. 1a, the fluid properties at the boundaries $K = 1$ and $K = KMAX$ are updated as the average of fluid properties at $K = 2$ and $K = KMAX$-1 for a symmetric flowfield.

For an unsymmetric flow, the periodicity on these boundaries does not exist. Therefore, in order to obtain the solution for such a case, the whole propfan should be solved. This is done by advancing the solution of each block one time step, one block at a time. In this case again the boundaries are updated explicitly, after the interior points have been updated. This is done by averaging the flow variables from the nodes on each side of the boundary from the adjoining blocks. Referring to Fig. 1b (the subscripts refer to the corresponding block), the quantities at boundary $K = KMAX$ of block N (which is also the boundary $K = 1$ for block $N + 1$) would be the average of flow quantities at $K = KMAX$-1 of block

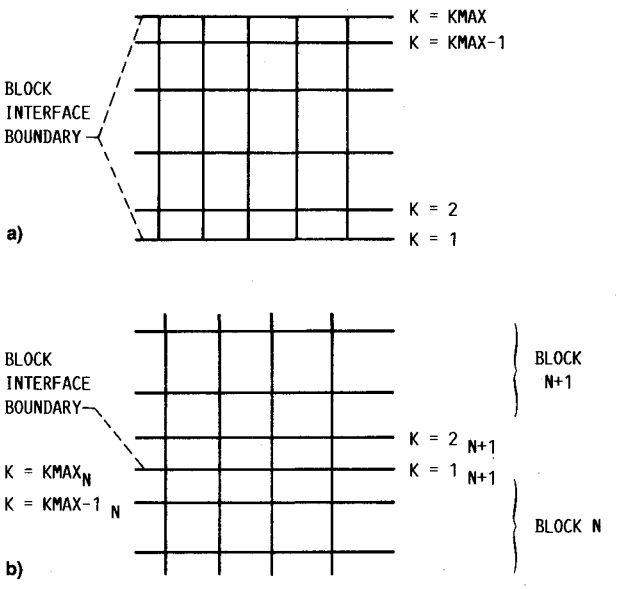

Fig. 1 Block interface boundaries.

N and $K = 2$ of block $N + 1$. In doing so, the latest available values at any given time are used.

Solution Procedure

The governing equations described earlier are solved using a hybrid scheme based on the ADI algorithm, described in next section. An implicit method is more demanding as far as coding is concerned. However, it allows larger time steps to be taken as opposed to the explicit schemes.

Time integration is carried out using the first-order accurate Euler implicit rule

$$\boldsymbol{q}^{n+1} = \boldsymbol{q}^n + \Delta\tau \frac{\partial \boldsymbol{q}^{n+1}}{\partial \tau} \quad (8)$$

where the superscript n denotes the current time level, at which the flow variables are known, and $(n + 1)$ the next or unknown time level. Even though this is a first-order accurate scheme, satisfactory time accuracy is obtained because a relatively small time step is required to maintain numerical stability.

Substituting the Euler Eq. (5) in Eq. (8), we get

$$\boldsymbol{q}^{n+1} = \boldsymbol{q}^n - \Delta\tau(\boldsymbol{E}_\xi + \boldsymbol{F}_\eta + \boldsymbol{G}_\zeta)^{n+1} \quad (9)$$

The partial derivatives $\boldsymbol{E}_\xi$, $\boldsymbol{F}_\eta$, and $\boldsymbol{G}_\zeta$ are obtained using the standard second-order accurate central differences.

The Hybrid Scheme

In order to decrease the computational time, flux terms in two directions (ξ, ζ) are treated implicitly while the radial direction (η) flux terms are treated semiexplicitly. This method requires only two costly inversions of the block tridiagonal matrix, in the two implicit directions. Rizk and Chaussee[15] first used this hybrid scheme with the Beam and Warming algorithm. Using this technique, the solver marches along the η direction, solving the equations one η plane at a time. The marching direction is reversed after every sweep, in order to remove any dependency on the marching direction. Equation (9) can then be rewritten as

$$\boldsymbol{q}^{n+1} = \boldsymbol{q}^n - \Delta\tau(\boldsymbol{E}_\xi^{n+1} + \boldsymbol{F}_\eta^{n,n+1} + \boldsymbol{G}_\zeta^{n+1}) \quad (10)$$

Since the η marching direction is changed every iteration, the $\boldsymbol{F}_\eta^{n,n+1}$ alternates between

$$\frac{\boldsymbol{F}_{i,j+1,k}^{n} - \boldsymbol{F}_{i,j-1,k}^{n+1}}{2\Delta\eta}$$

during the odd time steps, and

$$\frac{\boldsymbol{F}^{n+1}_{i,j+1,k} - \boldsymbol{F}^{n}_{i,j-1,k}}{2\Delta\eta}$$

during the even time steps.

The above discretization leads to a set of algebraic equations for $\boldsymbol{q}$. These equations are costly to solve since the flux vectors $\boldsymbol{E}$ and $\boldsymbol{G}$ are highly nonlinear. The nonlinearity is removed by linearizing the fluxes about the previous time step value, resulting in the following linear equation:

$$[I + \Delta\tau(\delta_\xi A^n + \delta_\zeta B^n)]\boldsymbol{q}^{n+1} = [I + \Delta\tau(\delta_\xi A^n + \delta_\zeta B^n)]\boldsymbol{q}^n + \boldsymbol{R}^{n,n+1} \quad (11)$$

where

$$\boldsymbol{R}^{n,n+1} = -\Delta\tau(\delta_\xi \boldsymbol{E}^n + \delta_\eta \boldsymbol{F}^{n,n+1} + \delta_\zeta \boldsymbol{G}^n) \quad (12)$$

and the operator notation $\delta_\xi(A\boldsymbol{q}) = [\delta_\xi A]\boldsymbol{q}$ and $\delta_\zeta(B\boldsymbol{q}) = [\delta_\zeta B]\boldsymbol{q}$ is used.

This Euler equation formulation can be very easily extended to solve the Navier-Stokes equations by simply adding the viscous terms to the right-hand side. It does not alter the numerical formulation.

Now defining $\Delta\boldsymbol{q}^{n+1} = \boldsymbol{q}^{n+1} - \boldsymbol{q}^n$, we can rewrite the Eq. (11) as

$$[I + \Delta\tau(\delta_\xi A^n + \delta_\zeta B^n)]\Delta\boldsymbol{q}^{n+1} = \boldsymbol{R}^{n,n+1} \quad (13)$$

Even though the governing equation has been linearized, Eq. (13) is still very difficult to solve, as the matrix operator on the left-hand side is very large and very sparse. However, the matrix operator can be approximately factorized as

$$[I + \Delta\tau(\delta_\xi A + \delta_\zeta B)] = [I + \Delta\tau\delta_\xi A][I + \Delta\tau\delta_\zeta B] + \mathcal{O}(\Delta\tau^2) \quad (14)$$

This factorization does not affect the temporal accuracy. Equation (13) can then be written as

$$[I + \Delta\tau\delta_\xi A^n][I + \Delta\tau\delta_\zeta B^n]\{\Delta\boldsymbol{q}^{n+1}\} = \boldsymbol{R}^{n,n+1} \quad (15)$$

or defining

$$\Delta\boldsymbol{q}^{*n+1} = [I + \Delta\tau\delta_\zeta B^n]\Delta\boldsymbol{q}^{n+1} \quad (16)$$

we get the following system of equation:

$$[I + \Delta\tau\delta_\xi A^n]\Delta\boldsymbol{q}^{*n+1} = \boldsymbol{R}^{n,n+1} \quad (17)$$

$$[I + \Delta\tau\delta_\zeta B^n]\Delta\boldsymbol{q}^{n+1} = \Delta\boldsymbol{q}^{*n+1} \quad (18)$$

These equations can be easily solved for $\Delta\boldsymbol{q}^{n+1}$ by performing two successive block tridiagonal inversions. Since the ξ and ζ directions are uncoupled, the two inversions are performed first with a ξ sweep and then with a ζ sweep, thus the name "alternating direction." These inversions are performed at each spanwise station, marching along the spanwise direction. As mentioned earlier, the marching direction is reversed every iteration. Each element of the block tridiagonal matrix has 5×5 elements.

Artificial Dissipation

The use of central difference makes the scheme mildly unstable, and also introduces odd-even decoupling. This is remedied by adding artificial dissipation. The implementation of artificial dissipation in the present work is based on the formulation of Jameson et al.[16] This scheme has a second-order implicit dissipation and a blend of second/fourth difference explicit dissipation terms. A scaling factor for both implicit and explicit dissipation is employed to control the amount of dissipation in the scheme. Adding the dissipation terms, Eqs. (17) and (18) can be written as

$$[I + \Delta\tau(\delta_\xi A^n + \varepsilon_I D_{I_\xi})]\Delta\boldsymbol{q}^{*n+1} = \boldsymbol{R}^{n,n+1} - \varepsilon_E D_E \Delta\tau \quad (19)$$

$$[I + \Delta\tau(\delta_\zeta B^n + \varepsilon_I D_{I_\zeta})]\Delta\boldsymbol{q}^{n+1} = \Delta\boldsymbol{q}^{*n+1} \quad (20)$$

D_{I_ξ}, D_{I_ζ}, and D_E are described in Ref. 17. ε_I and ε_E are user-supplied constants that depend on grid spacing. At the boundaries, the fourth-order differences are replaced by second-order differences.

Aeroelastic Model

As mentioned earlier, the propfan has thin, swept, and twisted blades. Since the blades are thin and flexible, deflections due to centrifugal and steady aeroloads are large. Hence, the aeroelastic problem is inherently nonlinear, requiring geometric nonlinear theory of elasticity.[18]

The blades have large sweep and twist, which couples blade bending and torsional motions. They behave like plate-like structures because of the low aspect ratio. These factors require a finite-element structural model that accounts for centrifugal softening and stiffening effects and, possibly, Coriolis effects. It has been found that the Coriolis effects are negligible for thin blades.[19] The centrifugal terms are important because of large blade sweep and flexibility. By assuming a rigid hub, the blades are structurally decoupled from one another. Consequently, it is sufficient to structurally model just one blade. Then, the governing aeroelastic equation can be written as

$$\{[K(\Omega)_s] + [K(u)]\}\{u\} = \{P(u)\} \quad (21)$$

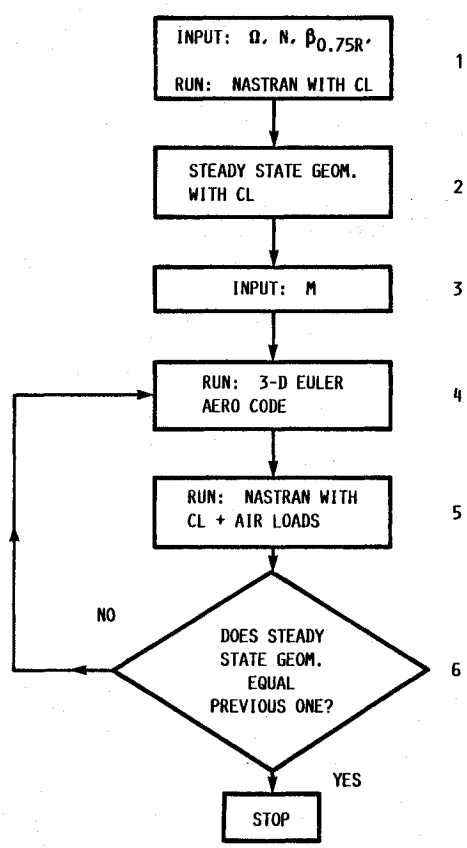

Fig. 2 Flowchart of the aeroelastic analysis.

$[K(\Omega)_s]$ is a function of the rotational speed Ω, and $[K(u)]$ is a function of the nodal displacements.

In the present paper, the geometric nonlinear analysis was performed using the MSC/NASTRAN,[20] in which the geometric nonlinear analysis is identified by "solution 64." The solution 64 uses a modified Newton-Raphson algorithm along with load updating to simulate the correct displacement-load relationship. It has the capability to update the displacement-dependent centrifugal forces. The solution sequence is controlled through "subcases" or iterations with a minimum of two being required. The first subcase computes the initial, linear-deflected shape. Subsequent subcases then use the previously deflected shape to compute the differential stiffness matrix along with the new set of displacements.[21]

The iterative method of solving Eq. (21) is shown in Fig. 2. Basically, a centrifugally deformed geometry is used to calculate steady aeroloads with the Euler solver described in the previous section. These aeroloads are then used to calculate a new deformed shape due to combined centrifugal and steady aeroloads. The process, steps 4–6, is repeated until a converged, deformed geometry is obtained.

Results and Discussion

The flow solutions obtained for two advanced propellers, namely SR3 and SR7L, are presented next. The calculations have been performed on a "hot shape," obtained by including the deflections due to centrifugal loading in the undeflected blade shape ("cold shape").

A body fitted H-O grid was used for these calculations. A typical grid used in the calculation is shown in Fig. 3. The domain of calculation was taken to be the region between two blades with upper surface of one blade and lower surface of the adjoining blade as the boundaries of the domain. This region is referred to as blade passage. In general, in order to model the influence of adjacent blades (cascade effect), the entire propfan with all of the blades (passages) need to be solved. However, for an axisymmetric flowfield considered here, all blade passages can be assumed to be identical, and only one blade passage need be solved enforcing the conditions of symmetry.

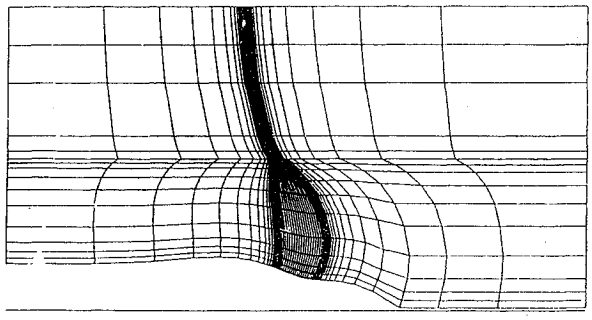

a) H-grid in streamwise plane.

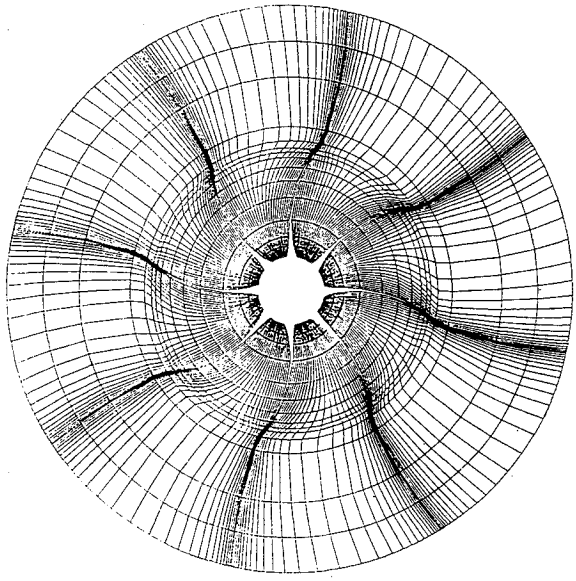

b) O-grid in azimuthal plane.

Fig. 3 Grids.

Blade Setting Angle Considerations

There is some uncertainty as to the blade-setting angle that should be used in these calculations. Experimental measurements may not be sufficiently reliable. During wind-tunnel tests at Modane[22] for the SR7L propfan, setting angle was adjusted to match the power coefficient of different runs for the same flight condition. Adjustments of as much as 2.6 deg were needed for some flight conditions. Furthermore, the helical wake behind the propeller induces an inflow through the propeller disc. Since no wake modeling is used in the present calculations, and only a portion of the wake is captured by the grid, the rest of the inflow must be accounted for in some consistent manner. Because of these reasons, in some of the cases discussed next, the power coefficients were matched with experimental measurements by adjusting the setting angle, through rigid-body rotation of the blade, about its pitch change axis.

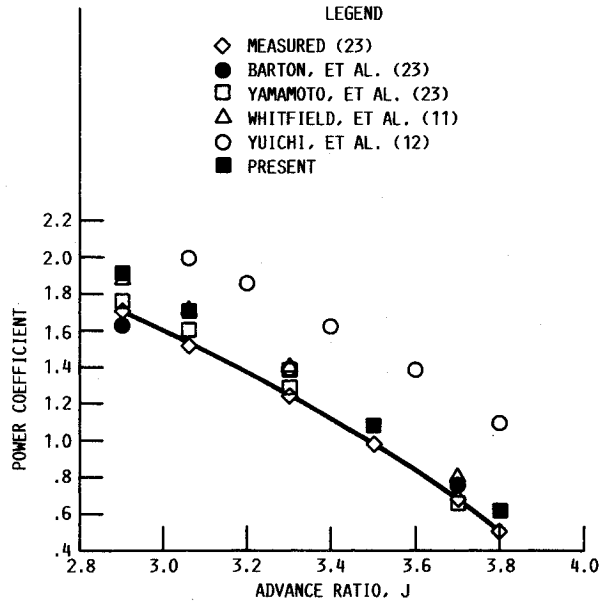

Fig. 4 Power coefficient vs advance ratio for SR3, eight-bladed propfan ($M_\infty = 0.8$).

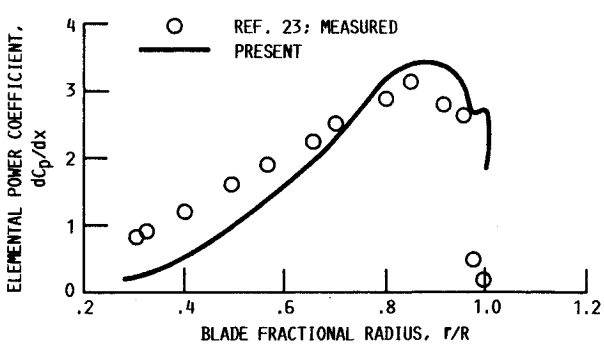

Fig. 5 Elemental power coefficient vs radius for SR3, eight-bladed propfan ($J = 3.002$; $M_\infty = 0.8$; $\beta = 60.5$ deg).

SR3 Propfan

The hybrid scheme, described earlier, was used to solve the flowfield around an 8-bladed SR3 propfan. The SR3 propfan was designed to operate at a freestream Mach number of 0.8, advance ratio of 3.06, at an altitude of 30,000 ft. Experimental data has been reported in Ref. 23, and the results obtained from the present analysis are compared in Figs. 4 and 5.

Figure 4 shows a comparison of the power coefficient of the propfan as a function of the advance ratio, with experimental data.[23] It also shows the comparison with other published numerical results.[11,12] No adjustments to the setting angle was made for this comparison. As can be seen the comparison with experiment is good; however, the power coefficients are consistently overpredicted. The results compare well with other published results, as well. As shown in Ref. 23, the power coefficients are quite sensitive to the blade-setting angle; however, an accurate measure of the blade-setting angle β is difficult. Also, since the blades are thin and somewhat flexible, they are susceptible to deformations under loading during operation. These deformations result in a modified twist distribution on the blade. Also, the viscous effects are not included in the present analysis. Any or all of these phenomena could contribute to the overprediction of the power coefficient.

The variation of elemental power coefficient with radial location is plotted and compared with experimental results in Fig. 5. In order to obtain a more meaningful comparison, the blade-setting angle was modified slightly in the numerical calculation, so as to match the experimental power coefficient. The power coefficient measured in the experiment was 1.385 for a freestream Mach number of 0.8, β setting angle of 60.7 deg, and the advance ratio of 3.002. The calculations were carried out with the freestream Mach number of 0.8, the setting angle of 58.5 deg, and the advance ratio of 3.002 to obtain the same power coefficient. As can be seen, a fairly good correlation is obtained; however, the elemental power is underpredicted for the inboard stations and overpredicted for the outboard stations. This is because the effect of the tip vortex is not properly accounted for. In these calculations no wake modeling is included, also the grid is not fine enough to properly capture the strength of the tip vortex. Capturing a weaker tip vortex results in smaller downwash velocity near the tip region, thus reaulting in an overprediction of blade loading near the tip. As the total power is matched with the experiment, an overprediction in the tip region results in an underprediction on the inboard region.

SR7L Propfan

The SR7L propfan has been designed for an operating freestream Mach number of 0.8, rotational speed of 1700 rpm, and at an altitude of 35,000 ft. In this section, calculations for a two-bladed SR7L propfan are presented. The aerodynamic calculations are first performed on the "hot shape." The effect of blade flexibility is then included in the calculations.

In Fig. 6, the elemental pressure coefficient difference is compared with experiment for a two-bladed SR7L propfan. The blade was operating at a freestream Mach number of 0.775 and advance ratio of 3.088. The setting angle was adjusted to match the power coefficient. The pressure coefficient difference ΔC_p ($C_{pl} - C_{pu}$) is plotted and compared against experimental data[22] at various span locations. The comparison is good, except near the leading edge on the outboard stations.

The effect of blade flexibility on performance was studied next for the SR7L propfan blade. The effect of flexibility is included by the aeroelastic iteration process, described earlier and shown in Fig. 2. It should be noted that in NASTRAN, the initial blade shape is always used to start the nonlinear analysis.

It is important that the blade finite-element model accurately reflect its structural characteristics, since the entire analysis process is centered around the stiffness matrix. The NASTRAN finite-element model used in this study is based on the final blade design.[24] The finite-element model of the SR7L blade is shown in Fig. 7. The model has 261 nodes and 449 triangular shell elements. Bar elements are used to model the shank. Multipoint constraint grid chords are used to define

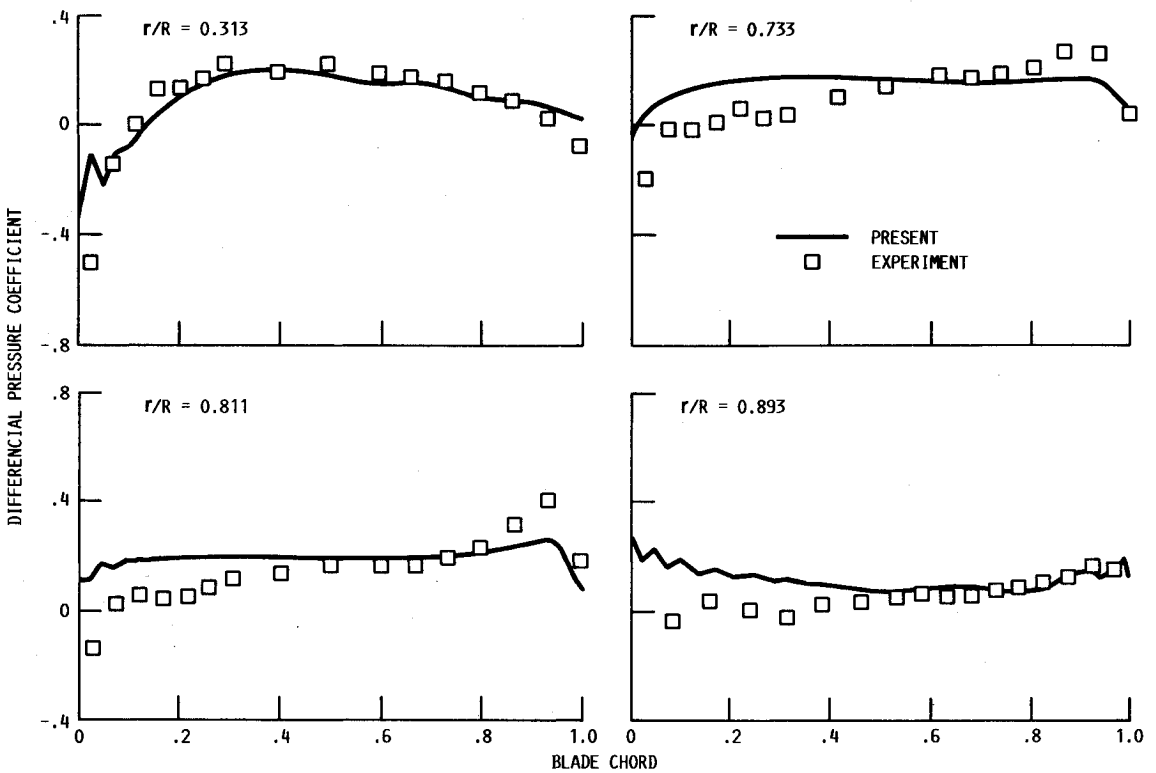

Fig. 6 Pressure coefficient difference at various radial locations for two-bladed SR7L propfan ($M_\infty = 0.775$; $J = 3.088$; $\beta = 54.6$ deg).

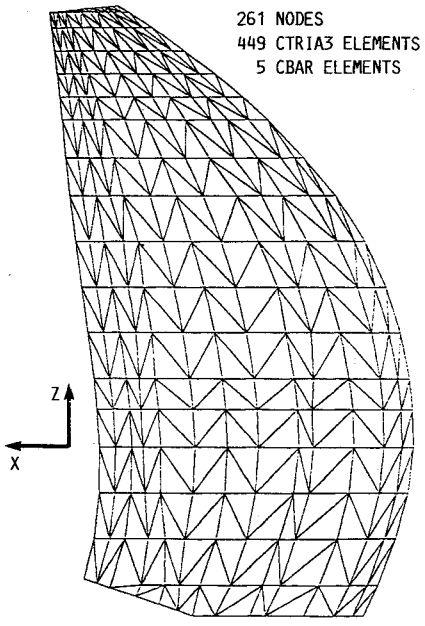

Fig. 7 SR7L propfan blade finite-element model.[21]

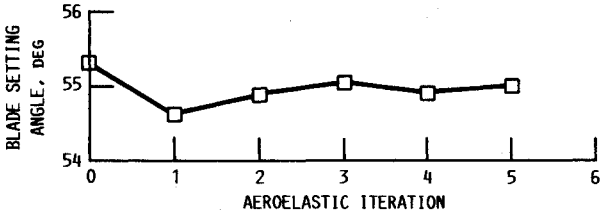

Fig. 8 Blade-setting angle at 75% span vs aeroelastic iteration for SR7L propfan (M_∞ = 0.775; J = 3.088).

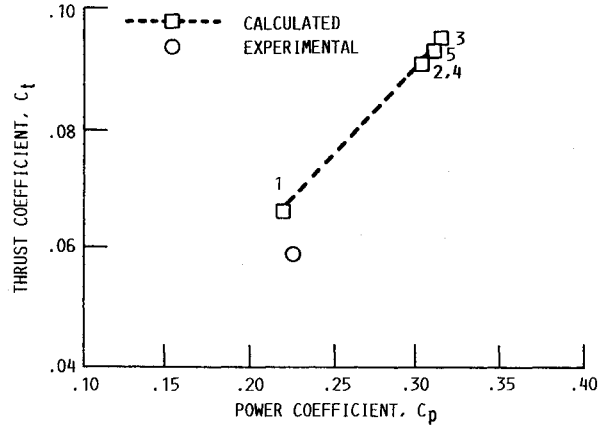

Fig. 9 Calculated thrust coefficient vs power coefficient for each aeroelastic iteration for a SR7L, two-bladed propfan (M_∞ = 0.775; J = 3.088).

the shank/blade interface.[25] The validity of the above finite-element blade model has been shown in Ref. 21.

The aeroloads obtained from the Euler solver are transferred to the NASTRAN grid for structural deformation calculations. The loads required as inputs to NASTRAN are the pressure differences at the centroids of the triangular element. As the two grids are not identical, an interpolation of the data was required. A spline interpolation was used to obtain the loads at the centroids of the elements. The deflections obtained from NASTRAN, under these loads, are then used to define the new blade shape. The loads are then recalculated

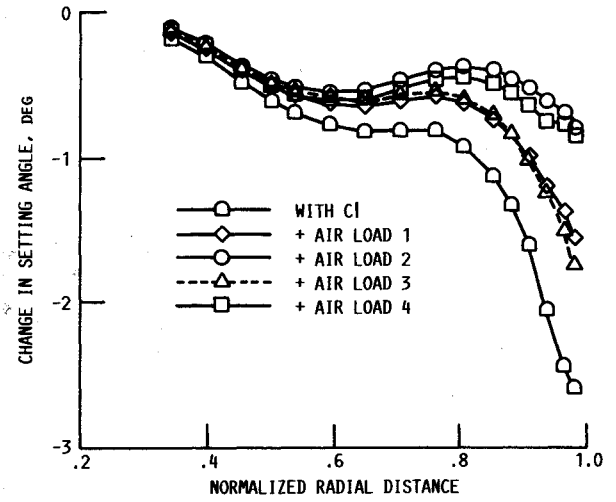

Fig. 10 Change in blade-setting angle vs blade span for SR7L propfan (M = 0.775; J = 3.088).

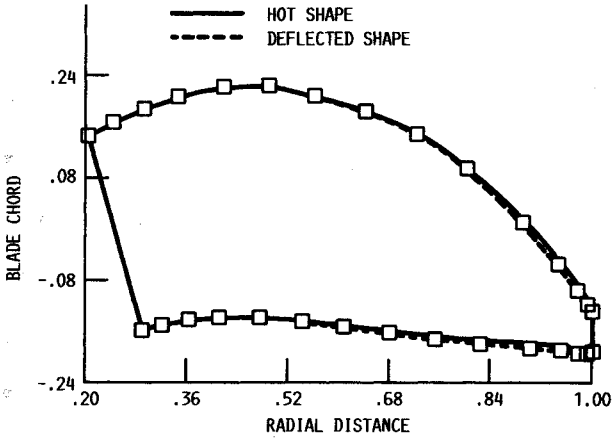

Fig. 11 In-plane deflection of blade planform for SR7L, two-bladed propfan (M_∞ = 0.775; J = 3.088; β = 54.6 deg).

for this new blade shape, and the process is repeated until convergence. The effect of the aeroelastic iteration on the calculation is shown in Figs. 8–12.

Figure 8 shows the blade-setting angle vs the iteration. The effect of centrifugal loads is seen as a change in the blade-setting angle from iteration 0 to iteration 1. It shows that the centrifugal loads reduce the blade-setting angle. This seems to be the largest effect on blade shape. Adding the deflections from centrifugal loads to the blade shape gives the blade shape known as "hot shape." The loads obtained from this shape are then again used to obtain the new deflected shape. This iteration has been continued until the changes in power coefficient became reasonably small, and the setting angle had converged to within 0.1 deg.

In Fig. 9, the thrust coefficient is plotted against the power coefficient for subsequent iterations. The experimental point is also plotted. The power coefficient obtained from the hot shape (marked 1) compares well with the experiment. However, the power coefficient changes considerably (marked 2 to 5) as the blade is allowed to deform under this load. It can be seen from Figs. 8 and 9 that the initial change in shape leads to large changes in power coefficient. For this particular case, under which the blades are loaded heavily, almost 40% change in power coefficient is observed when the effect of aerodynamic loading is included in the blade shape. It can be seen from Fig. 9 that further iterations would not have provided any significantly new understanding of the effect of flexibility on the performance.

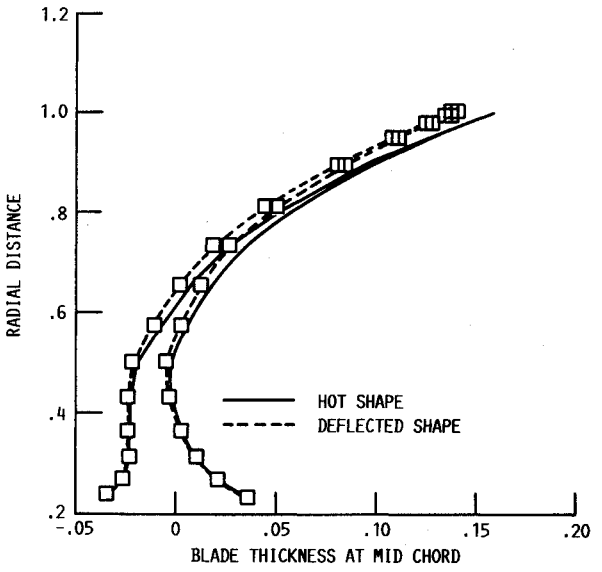

Fig. 12 Out-of-plane deflection at midchord for SR7L, two-bladed propfan (M_∞ = 0.775; J = 3.088; β = 54.6 deg).

In Fig. 10, the relative change, from "cold shape," in twist angle over the span is plotted. This shows that the largest deflection occurs near the tip, with practically no deflection on the root sections. Also it should be noted that the variation in the blade twist is nonlinear and is largest near the tip. It is also evident from this figure that the change in blade twist near the tip shows larger oscillation between iterations than the setting angle, as shown in Fig. 8. This implies that adjustments and conclusions based on setting angle alone can be misleading. Also, for the heavily loaded blade, as considered here, further iterations are required for convergence in blade shape. This clearly shows that for better performance calculations, structural flexibility should be included in the analysis.

Figure 11 shows the in-plane deflection of the deflected blade planform, and Fig. 12 shows the out-of-plane deflection of the deflected blade at constant chord. Again, the largest deflection is towards the tip, with practically no deflection towards the root. Figures 10–12 show clearly that rigidly rotating the blade to match the power coefficient does not simulate the correct blade shape. Also, as seen from Fig. 9 for highly loaded blades, these small differences might change the loading considerably. Thus, arriving at the final blade shape might be critical for vibration and flutter calculations as well. Hence, in order to obtain a better comparison with experimental power coefficient, load distribution on blade, and the deflected blade shape, the blade-setting angle should be chosen properly. This requires some trial and error in selecting the "cold" or "hot" shape from which the aeroelastic iteration should be started.

Computer Requirements

All of the above computations were performed on the CRAY XMP24 computer available at NASA Lewis Research Center. For a grid size of 70 × 35 × 27, the total memory and CPU time per time step required were 1.8 MW and 2.4 s, respectively. The NASTRAN run required 100 cpu seconds for 261 nodes, for each structural integration.

Concluding Remarks

This study showed that the hybrid scheme can be applied successfully to a propfan configuration (low aspect ratio, highly swept, and very thin blades). It also shows that the calculated power coefficient and elemental power coefficient variation with radius for SR3 showed good correlation with experiment, and the pressure coefficient difference for SR7L agreed well with measured values. Furthermore, the effect of aeroloads is to compensate for the untwisting due to centrifugal loads, and the effect of steady aeroloads on blade deflections can be significant and should be included in the aeroelastic analysis.

Additional improvements to this work are clearly needed. The calculations presented here must be repeated on denser grids to assess the effects of grid density, especially the ability to capture an accurate vortex wake. Adjusting the setting angle without accounting for blade deflection might work well for predicting the integrated performance quantities, but is clearly not sufficient for aeroelastic purposes. Also, a way of choosing the setting angle for the "cold shape," without an iterative approach, must be developed such that the converged shape and performance quantities compare well with experiment.

Acknowledgments

The authors wish to acknowledge Dr. Richard August of Sverdrup Technology Inc., Cleveland, Ohio, for many helpful suggestions. This work was carried out under NASA Grant NAG3-730 from NASA Lewis Research Center in Cleveland, Ohio. Mr. George L. Stefko was the grant monitor.

References

[1]Whitlow, J. B., Jr., and Sievers, G. K., "Fuel Savings Potential of the NASA ATP," NASA TM-83736, Sept. 1984.

[2]Mehmed, O., and Kaza, K. R. V., "Experimental Classical Flutter Results of a Composite Advanced Turboprop Model," NASA TM-88792, July 1986.

[3]Goldstein, S., "On the Vortex Theory of Screw Propellers," *Royal Society (London) Proceedings*, Vol. 123, No. 792, April 1929, pp. 440–465.

[4]Sullivan, J. P., "The Effect of Blade Sweep on Propeller Performance," AIAA Paper 77-176, June 1977.

[5]Egolf, T. A., Anderson, O. L., Edwards, D. E., and Landgrebe, A. J., "An Analysis for High-Speed Propeller-Nacelle Aerodynamic Performance Prediction: Vol. 1—Theory and Initial Application, and Vol. 2—User's Manual for the Computer Program," United Technologies Research Center, R79-912949-19, June 1979.

[6]Hanson, D. B., "Compressible Lifting Surface Theory for Propeller Performance Calculation," *Journal of Aircraft*, Vol. 22, No. 1, Jan. 1985, pp. 19–27.

[7]Williams, M. H., and Hwang, C., "Three-Dimensional Unsteady Aerodynamics and Aeroelastic Response of Advanced Turboprops," AIAA Paper 86-0846, May 1986.

[8]Jou, W. H., "Finite-Volume Calculation of the Three-Dimensional Flow Around a Propeller," AIAA Paper 82-0957, June 1982.

[9]Jameson, A., and Caughy, D. A., "A Finite-Volume Method for Transonic Potential Flow Calculations," AIAA Paper 77-635, June 1977.

[10]Chaussee, D. S., "Computation of Three-Dimensional Flow Through Prop Fans," Nielsen Engineering and Research Inc., NEAR TR-199, June 1979.

[11]Whitfield, D. L., Swafford, T. W., Janus, J. M., Mulac, R. A., and Belk, D. M., "Three-Dimensional Unsteady Euler Solutions for Propfans and Counter-Rotating Propfans in Transonic Flow," AIAA Paper 87-1197, June 1987.

[12]Matsuo, Y., Arakawa, C., Saito, S., and Kobayashi, H., "Navier-Stokes Computations for Flowfield of an Advanced Turboprop," AIAA Paper 88-3094, July 1988.

[13]Bober, L. J., and Mitchell, G. A., "Summary of Advanced Methods for Predicting High-Speed Propeller Performance," NASA TM-81409, Jan. 1980.

[14]Lax, P. D., "Weak Solutions of Nonlinear Hyperbolic Equations and their Numerical Computation," *Communications in Pure and Applied Mathematics*, Vol. 7, No. 1, Feb. 1954, pp. 159–193.

[15]Rizk, Y. M., and Chaussee, D. S., "Three-Dimensional Viscous-Flow Computations Using a Directionally Hybrid Implicit-Explicit Procedure," AIAA Paper 83-1910, July 1983.

[16]Jameson, A., Schmidt, W., and Turkel, E., "Numerical Solutions of the Euler Equations by Finite-Volume Methods Using Runge-Kutta Time-Stepping Schemes," AIAA Paper 81-1259, June 1981.

[17]Wake, B. E., and Sankar, L. N., "Solutions of the Navier-Stokes Equations for the Flow About a Rotor Blade," *Journal of the Amer-*

ican Helicopter Society, Vol. 34, No. 2, April 1989, pp. 13–23.

[18]Kaza, K. R. V., Mehmed, O., Naraynan, G. V., and Murthy, D. V., "Analytical Flutter Investigation of a Composite Propfan Model," *Journal of Aircraft*, Vol. 26, No. 8, Aug. 1989, pp. 772–780.

[19]Subramanyam, K. B., Kaza, K. R. V., Brown, G. V., and Lawrence, C., "Nonlinear Bending-Torsional Vibration and Stability of Rotating, Pretwisted, Preconed Blades Including Coriolis Effects," NASA TM 87207, Jan. 1986.

[20]Lawrence, C., Aiello, R. A., Ernst, M. A., and McGee, O. G., "A NASTRAN Primer for the Analysis of Rotating Flexible Blades," NASA TM89861, May 1987.

[21]August, R., and Kaza, K. R. V., "Vibration, Performance, and Flutter Response Characteristics of a Large-Scale Propfan and Its Aeroelastic Model," AIAA Paper 88-3155, July 1988.

[22]Bushnell, P., "Measurement of the Steady Surface Pressure Distribution on a Single Rotation Large-Scale Advanced Propfan Blade at Mach numbers from 0.03–0.78," NASA CR-182124, July 1988.

[23]Rohrbach, C., Metzger, F. B., Black, D. M., and Ladden, R. M., "Evaluation of Wind-Tunnel Performance Testings of an Advanced 45-Deg Swept Eight-Bladed Propeller at Mach Numbers from 0.45–0.85," NASA CR-3505, March 1982.

[24]Sullivan, W. E., Turnberg, J. E., and Violette, J. A., "Large-Scale Advanced Propfan (LAP) Blade Design," NASA CR-174790, March 1984.

[25]Aiello, R. A., Chi, S., "Advanced Composite Turboprops: Modelling, Structural and Dynamic Analyses," ASME Paper 87-GT-78, July 1987.